Nonlinear three-mode interaction and drift-wave turbulence in a tokamak edge plasma

A. M. Batista and I. L. Caldas
Instituto de Física, Universidade de São Paulo, Caixa Postal 66318, 05315-970, São Paulo, SP, Brazil

S. R. Lopes and R. L. Viana
Departamento de Física, Universidade Federal do Paraná, 81531-990, Curitiba, Paraná, Brazil

W. Horton and P. J. Morrison
Department of Physics and Institute for Fusion Studies, The University of Texas at Austin, Austin, Texas, 78712

A three-wave interaction model with quadratic nonlinearities and linear growth/decay rates is used to investigate the occurrence of drift-wave turbulence driven by pressure gradients in the edge plasma of a tokamak. Model parameters are taken from a typical set of measurements of the floating electrostatic potential in the tokamak edge region. Some aspects of the temporal dynamics exhibited by the three-wave interaction model are investigated, with special emphasis on a chaotic regime found for a wide range of the wave decay rate. An intermittent transition from periodic to chaotic behavior is observed and some statistical properties, such as the interburst and laminar length interval durations, are explored. © *2006 American Institute of Physics*. [DOI: 10.1063/1.2184291]

I. INTRODUCTION

For a long time, a major goal in the study of high-temperature plasmas in toroidal magnetic confinement systems has been to understand the causes and associated rates of anomalously large cross-field transport.[1] A considerable number of theories have been developed to identify the underlying turbulence mechanisms thought to cause this anomalous transport.[2,3] Clearly, understanding plasma turbulence is a key component needed in order to determine transport properties.[4] Such turbulent processes often display a broad fluctuation spectra with maxima at the longest measured scales (small wave vectors and high frequencies).[5] Because wave-like instabilities occur for a finite range of the spectrum, nonlinear mechanisms such as three- or four-wave interaction are essential for explaining the broadband plasma instabilities observed in astrophysical and laboratory settings.[6,7]

Drift waves play an important role in the physics of transport in the strongly magnetized plasmas that occur in tokamaks.[5] For such high-temperature plasmas, the presence of sufficiently steep density gradients in the plasma edge can give rise to fully developed drift-wave turbulence, which is considered a likely candidate for explaining the observed anomalous transport rates.[5] Hasegawa and Mima obtained a nonlinear partial differential equation for describing drift-wave propagation and the emergence of cross-field transport in tokamak plasmas.[8] This equation has been the starting point for many investigations of the modulational instability of a monochromatic drift wave, a wave that grows linearly until it reaches a threshold, at which point it decays and generates two coupled sidebands.[9,10]

The Hasegawa and Mima equation has spawned additional models such as the three-wave model introduced by Horton and Hasegawa.[9] In the present work we add to the

Horton and Hasegawa model phenomenological growth/decay rates for the three waves, in order to simulate the energy redistribution among different modes. Energy-transfer processes are key ingredients needed to explain the observed broadband spectrum of the drift-wave turbulence in the tokamak plasma edge.[4] The three wave vectors have been chosen so that one of them is a dominant mode and the other two are sidebands that complete a triplet in accordance with a specific resonance condition. Previously this model successfully described wave–wave interactions in a context of astrophysical interest.[11] The coupling strength increases with the introduction of the phenomenological growth/decay rates, and the choice for these values in the present work is based on measurements of the floating electrostatic potential at the plasma edge in the small Brazilian tokamak, Tokamak Brasileiro (TBR).[12] However, our results are applicable to a wide range of small tokamaks with similar characteristics.

The dynamics of the three-wave model will be analyzed with special emphasis on the chaotic regimes found for wide ranges of the linear growth/decay rates. One of the routes to chaos found in this model is intermittency between chaotic bursting and stable periodic motion, a common behavior preceding the development of large-scale turbulence.[13,14] Statistical properties of these intermittent and bursting regimes are then studied in order to provide a characterization of the transition to drift-wave turbulence. Scaling laws are derived from time series obtained from our model, which can be compared with experimental results so as to indicate possible regimes involving the transition to drift-wave turbulence.

The rest of the paper is organized as follows: in Sec. II we introduce our notation and review the theoretical arguments leading to the Hasegawa-Mima equation, as well as its modal truncation to a three-wave model. Because we have added the growth and decay rates, in Sec. III we present a standard linear analysis of this model in order to highlight

13, 042510-1

some features that we shall meet in the numerical analyses of the full nonlinear model. The estimation of model parameters based on tokamak parameters is described in Sec. IV. Section V displays numerical results for the dynamics generated by the three-wave model, with emphasis on the chaotic regime that is taken to be a caricature of the fully spatiotemporal turbulent scenario. The statistical properties of bursting events are treated in Sec. VI. The last section, Sec. VII, is devoted to our conclusions.

II. BACKGROUND

The description of drift-wave turbulence by the Hasegawa-Mima equation begins by supposing the propagation of an electrostatic wave at a frequency ω in a magnetized and inhomogeneous plasma.[9] The wave frequency is assumed to be much smaller than the ion-cyclotron frequency $\omega_{ci} = eB/m_i$, where m_i is the mass of the ions. The magnetic field is assumed to point in the positive z direction, $\mathbf{B} = B\hat{\mathbf{z}}$, and n_0 is the background plasma density. A linear wave exists in this situation if the phase velocity along the magnetic field satisfies the inequalities $v_{T_i} < (\omega/k_z) < v_{T_e}$, where v_{T_s} is the thermal velocity for ions ($s=i$) and electrons ($s=e$). For long wavelengths this is a drift wave, for which the dispersion relation is $\omega = \mathbf{k} \cdot \mathbf{v}_d$, where $\mathbf{v}_d$ is the diamagnetic drift velocity. Moreover, drift waves possess a characteristic dispersion scale length $\rho_s = \sqrt{T_e/m_i}/\omega_{ci}$.

We also suppose that the ion temperature T_i is much smaller than the electron temperature T_e, such that it suffices to consider the ion dynamics only and to describe the ions in terms of a fluid velocity $\mathbf{v}$. The scale length ρ_s is the fundamental electric cross-field shielding distance for charge clumps in the regime of drift-wave fluctuations. The distance arises from parallel electron currents flowing into and out of the charged regions and closing across the field by the polarization current $j_p = (n_i m_i/B^2)(dE_\perp/dt)$. For a cold plasma with $T_e \gg T_i$, as is the case for the experiments considered, the ion-diamagnetic term is negligible. The cross-field quasineutrality equation has a form analogous to that for Debye shielding with the shielding distance given by ρ_s.

The drift wave is characterized by an electrostatic potential, ϕ, with $\mathbf{E} = -\nabla\phi$, and the fluid equations relevant to this situation are the ion density conservation law and the force law with a Lorentz force corresponding to the drift wave. The plasma quasineutrality condition amounts to the ion density being equal to the electron density, with the latter satisfying a Boltzmann distribution $n \approx n_e = n_0 \exp(e\phi/T_e)$. To obtain a closed set of equations it is necessary to consider an equation for the vorticity of the ion motion, $\Omega = \nabla \times \mathbf{v}$, because a drift wave is actually a vortex-like mode. In the drift-wave description we suppose that the vorticity is much less than the ion-cyclotron frequency, so that the ratio $\epsilon = |\Omega|/\omega_{ci}$ can be used as a small expansion parameter in the calculations.

Introducing the following nondimensional variables:

$$x' := \frac{x}{\rho_s}, \quad y' := \frac{y}{\rho_s}, \quad t' := \omega_{ci}t, \quad \phi' := \frac{e\phi}{T_e}, \quad (1)$$

the set of equations describing the ion fluid motion in the drift-wave approximation can be combined to give the Hasegawa-Mima equation[8]

$$\frac{\partial}{\partial t}(\nabla^2\phi - \phi) - [(\nabla\phi \times \hat{\mathbf{z}}) \cdot \nabla]\left[\nabla^2\phi - \ln\left(\frac{n_0}{\omega_{ci}}\right)\right] = 0, \quad (2)$$

where the operator ∇ in the above equation denotes the gradient in the directions transverse to the magnetic field, $\nabla = \hat{\mathbf{x}}\partial/\partial x + \hat{\mathbf{y}}\partial/\partial y$. Here we dropped the primes for the nondimensional variables and for the sake of notational simplicity we do this henceforth.

The electrostatic turbulence in the tokamak plasma edge is thought to be driven by plasma density gradients. For low-beta plasmas it is reasonable to neglect magnetic-field inhomogeneities, and this is done. Having a density gradient which is compatible with the propagation of drift waves, their dispersion relation is given by[9]

$$\omega = \omega_k = \frac{1}{1+k^2}\left[(\mathbf{k} \times \hat{\mathbf{z}}) \cdot \nabla \ln\left(\frac{n_0}{\omega_{ci}}\right)\right] := \frac{\omega_*}{1+k^2}, \quad (3)$$

where ω is the drift-wave frequency and $\mathbf{k}$ is the wave vector in the direction perpendicular to the magnetic field. In the long-wavelength approximation, $k^2 \ll 1$, the drift-wave frequency reduces to the known expression $\omega_k = \mathbf{k} \cdot \mathbf{v}_d \equiv \omega_*$, where $\mathbf{v}_d$ is the diamagnetic drift velocity. The dimensionless k is obtained by scaling the wave vector with ρ_s, such that Eq. (3) is used for the dimensionless $k \gg 1$ for the cold ion plasma with $T_i/T_e \ll 1$.

To analyze the spectrum we Fourier-expand the electrostatic potential,

$$\phi(\mathbf{x},t) = \frac{1}{2}\sum_{k=1}^{\infty} [\phi_\mathbf{k}(t)\exp(i\mathbf{k} \cdot \mathbf{x}) + \phi_\mathbf{k}^*(t)\exp(-i\mathbf{k} \cdot \mathbf{x})], \quad (4)$$

where the $\phi_\mathbf{k}(t)$ are the electrostatic modes in Fourier space. Using energy and entropy conservation Hasegawa obtained the following stationary spectrum for these modes:[15]

$$\langle|\phi_\mathbf{k}|^2\rangle = \frac{W_k}{1+k^2} \sim \frac{1}{(\alpha+\beta k^2)(1+k^2)}, \quad (5)$$

where $W_k = (\alpha+\beta k^2)^{-1}$ is the energy spectrum.

Substituting (4) into the Hasegawa-Mima equation (2) yields an infinite system of coupled differential equations for the Fourier modes[9,16]

$$\frac{d\phi_\mathbf{k}}{dt} + i\omega_\mathbf{k}\phi_\mathbf{k} = \sum_{\mathbf{k}_\alpha,\mathbf{k}_\beta,\mathbf{k}_\gamma} \Lambda_{\mathbf{k}_\beta,\mathbf{k}_\gamma}^{\mathbf{k}_\alpha}\phi_{\mathbf{k}_\beta}^*\phi_{\mathbf{k}_\gamma}^*, \quad (6)$$

where the summation is over wave vectors that satisfy the triplet relation

$$\mathbf{k}_\alpha + \mathbf{k}_\beta + \mathbf{k}_\gamma = \mathbf{0}, \quad (7)$$

for any choice of $\mathbf{k}$. The drift-wave mode frequencies are given by the dispersion relation (3), and the coupling coefficients are given by

$$\Lambda_{\mathbf{k}_\beta,\mathbf{k}_\gamma}^{\mathbf{k}_\alpha} = \frac{(k_\gamma^2 - k_\beta^2)}{2(1+k_\alpha^2)}(\mathbf{k}_\beta \times \mathbf{k}_\gamma) \cdot \hat{\mathbf{z}}. \tag{8}$$

A central question of turbulence theory is how many of the infinite number of Fourier modes, $\phi_\mathbf{k}$, are necessary to adequately describe drift-wave turbulence. Studies of other nonlinear partial differential equations, such as the Zakharov and nonlinear Schrödinger equations, suggest it suffices to analyze a few modes when the turbulence is not yet fully developed.[17] For such situations of weak turbulence, it has been found that three modes can be sufficient to describe physically interesting scenarios. From the dynamical systems point of view it is necessary to use at least three Fourier modes, because an autonomous three-dimensional flow can exhibit chaotic solutions.[14]

An example that illustrates the worth of low-mode truncations is provided by the Lorenz equations that describe gravity forced convection of a fluid heated from below. This system arises from a parent system of equations that is likewise infinite dimensional.[18] However, for situations with fully developed turbulence, the fact that small-scale phenomena cannot be overlooked forces one to consider more and more modes as energy flows to arbitrarily fine scales, in accordance with Kolmogorov's theory.[13]

With these observations in mind, we proceed to our three-wave truncation, which we suppose has wave vectors $\mathbf{k}_1$, $\mathbf{k}_2$, and $\mathbf{k}_3$ satisfying the triplet condition (7), $\mathbf{k}_1 + \mathbf{k}_2 + \mathbf{k}_3 = 0$. Also, following Terry and Horton[19] we introduce phenomenological dissipative terms that describe mode growth or decay, in the form $\gamma_i \phi_{\mathbf{k}_i}$, for $i = 1, 2, 3, \ldots$, where γ_i are growth/decay coefficients. Truncating the coupled system of (6) with the incorporation of the dissipative terms gives

$$\frac{d\phi_1}{dt} + i\omega_1\phi_1 = \Lambda_{2,3}^1\phi_2^*\phi_3^* + \gamma_1\phi_1, \tag{9}$$

$$\frac{d\phi_2}{dt} + i\omega_2\phi_2 = \Lambda_{3,1}^2\phi_3^*\phi_1^* + \gamma_2\phi_2, \tag{10}$$

$$\frac{d\phi_3}{dt} + i\omega_3\phi_3 = \Lambda_{1,2}^3\phi_1^*\phi_2^* + \gamma_3\phi_3, \tag{11}$$

where for simplicity we have introduced the following notation:

$$\phi_j(t) = \phi_{\mathbf{k}_j}(t), \quad \omega_j = \omega_{\mathbf{k}_j}, \quad j = 1, 2, 3. \tag{12}$$

From Eq. (8) the coupling coefficients are seen to be

$$\Lambda_{\mathbf{k}_2,\mathbf{k}_3}^{\mathbf{k}_1} = \Lambda_{2,3}^1 = \frac{(k_3^2 - k_2^2)}{2(1+k_1^2)}(\mathbf{k}_2 \times \mathbf{k}_3) \cdot \hat{\mathbf{z}}, \tag{13}$$

$$\Lambda_{\mathbf{k}_3,\mathbf{k}_1}^{\mathbf{k}_2} = \Lambda_{3,1}^2 = \frac{(k_1^2 - k_3^2)}{2(1+k_2^2)}(\mathbf{k}_3 \times \mathbf{k}_1) \cdot \hat{\mathbf{z}}, \tag{14}$$

$$\Lambda_{\mathbf{k}_1,\mathbf{k}_2}^{\mathbf{k}_3} = \Lambda_{1,2}^3 = \frac{(k_2^2 - k_1^2)}{2(1+k_3^2)}(\mathbf{k}_1 \times \mathbf{k}_2) \cdot \hat{\mathbf{z}}. \tag{15}$$

Within this three-wave approximation, the Fourier expansion of the electrostatic potential is given by

$$\phi(\mathbf{x},t) = \tfrac{1}{2}[\phi_1(t)\exp(i\mathbf{k}_1 \cdot \mathbf{x}) + \phi_2(t)\exp(i\mathbf{k}_2 \cdot \mathbf{x})$$
$$+ \phi_3(t)\exp(i\mathbf{k}_3 \cdot \mathbf{x}) + \text{c.c.}]. \tag{16}$$

III. LINEAR ANALYSIS

Our approach to turbulence concerns the study of the energy flow among different modes, and we are particularly interested in analyzing how a given mode can transfer energy to the other ones. To this end we set the wave vectors of the three modes so that $k_1 \leq k_2 \leq k_3$, where k_2 stands for the inductor or pump wave, which generates sideband or daughter modes with wave numbers k_1 and k_3, respectively. Hence, the mode $\mathbf{k}_2$ is considered to be more excited than $\mathbf{k}_1$ and $\mathbf{k}_2$, which amounts to the condition $|\phi_2| \gg |\phi_{1,3}|$.

Before embarking on a numerical analysis of the nonlinearities involved in the evolution of the modes, we consider here a linear stability analysis in which the parameters $\gamma_1 = \gamma_2 = \gamma_3 \equiv 0$. In the following, the pump mode is assumed to have a constant amplitude A_2, whereas the two daughter modes evolve in time such that

$$\phi_1(t) = A_1(t)e^{-i\omega_1 t}, \tag{17}$$

$$\phi_2(t) = A_2 e^{-i\omega_2 t}, \tag{18}$$

$$\phi_3(t) = A_3(t)e^{-i\omega_3 t}. \tag{19}$$

Differentiating Eq. (17) with respect to time and substituting the result into Eq. (9) results in

$$\frac{dA_1}{dt} = \Lambda_{2,3}^1 A_2^* A_3^* e^{i\Delta\omega t}, \tag{20}$$

where $\Delta\omega := \omega_1 + \omega_2 + \omega_3$ is the frequency mismatch between the inductor wave and its two sideband modes. Analogously, we find the following for mode 3:

$$\frac{dA_3}{dt} = \Lambda_{1,2}^3 A_1^* A_2^* e^{i\Delta\omega t}. \tag{21}$$

Now differentiating Eq. (20) again and using Eq. (21) we obtain

$$\frac{d^2A_1}{dt^2} - i\Delta\omega\frac{dA_1}{dt} - \Lambda_{2,3}^1\Lambda_{1,2}^3|A_2|^2 A_1 = 0. \tag{22}$$

Assuming $A_1 \sim e^{pt}$, we determine the following two eigenvalues:

$$p = \frac{1}{2}\{i\Delta\omega \pm \sqrt{-(\Delta\omega)^2 + 4\Lambda_{2,3}^1\Lambda_{1,2}^3|A_2|^2}\} = i\left(\frac{\Delta\omega}{2}\right) \pm \Gamma, \tag{23}$$

where

$$\Gamma = \sqrt{-\left(\frac{\Delta\omega}{2}\right)^2 + \Lambda_{2,3}^1\Lambda_{1,2}^3|A_2|^2}. \tag{24}$$

Hence, if A_2 is kept constant, the daughter modes A_1 and A_3 can grow (decay) exponentially at a rate Γ when the pump

amplitude A_2 exceeds the frequency mismatch according to $|A_2|^2 > (\Delta\omega/2)^2 (\Lambda_{2,3}^1 \Lambda_{1,2}^3)^{-1}$. In our numerical simulations this condition is easily fulfilled because we estimate $|A_2|^2 > 10^{-4}$ using experimental results.

IV. APPLICATION TO TOKAMAK EDGE PLASMAS

In order to more fully explore the role of the nonlinear terms of Eqs. (9)–(11), we resort to numerical integration. In preparation for these calculations (described in Sec. V) we now discuss parameter values. To facilitate comparison with experimental results, we use parameter values extracted from data from a set of typical measurements made on the small Brazilian tokamak TBR. For this machine the toroidal field $B=0.4$ T, the central electron temperature $T_e=10$ eV, and the central electron density $n_0=7\times10^{18}$ m^{-3} (Refs. 20 and 21). A number of probes have been developed by the TBR team to measure the particle density and temperature fluctuations in the edge region, as well as to measure the particle confinement time.[20] The experimental results for TBR suggest that the turbulent transport is mainly electrostatic in nature,[21] and similar observations have been made on other tokamaks.[22]

For the TBR plasma, we estimate the ion-cyclotron frequency to be 3.82×10^7 Hz and the length scale $\rho_s\approx10^{-3}$ m. These values turn out to be compatible with those of other machines, such as the TEXT[23] and PLT[24] tokamaks. The radial density gradient at the plasma edge was estimated,[25] on the basis of particle flux measurements, to be

$$\mathcal{N} := \rho_s \left| \nabla \ln\left(\frac{n_0}{\omega_{ci}}\right) \right| = \rho_s \left| \frac{\nabla n_0}{n_0} \right| \approx 0.17. \quad (25)$$

Moreover, measurements of potential edge fluctuations using a triple electrostatic probe indicate a poloidal wave number k_θ in the range of $(1-5)\times10^3$ m^{-1}, with broad spectral content in the kHz range and a more pronounced feature at $\omega_{exp}\approx50$ kHz (Ref. 21).

We suppose a large aspect ratio geometry for the tokamak, such that the curvature effects are negligible in both toroidal and poloidal directions. This enables us to use "slab" geometry where the rectangular coordinates (x,y,z) stand for the radial position measured from the tokamak wall, and the rectified poloidal and toroidal angles, respectively. Accordingly we choose the wave-vector components k_{ix}, k_{iy}, and k_{iz}, with $i=1,2,3$, as being oriented along the radial, poloidal, and toroidal directions, respectively. Without loss of generality we assume the z components of the three wave vectors to vanish. This means the matching condition, $\mathbf{k}_1+\mathbf{k}_2+\mathbf{k}_3=\mathbf{0}$, defines a vector triangle in a constant-z plane, which is a surface of section transverse to the toroidal coordinate.

The experimental value of the dominant poloidal wave number of plasma edge fluctuations is taken to be our input value $k_{1y}=k_\theta=5\times10^3$ m^{-1}, which corresponds to a normalized value of $k_{1y}=5$. We are thus left with five unknown components of the wave vectors involved in the triplet. For convenience we assume the following linear relations between the wave-vector components:

$$k_{1x}=c_{11}k_{1y}, \quad k_{2x}=c_{22}k_{1y}, \quad k_{3x}=c_{33}k_{1y},$$
$$k_{2y}=c_{32}k_{1y}, \quad k_{3y}=c_{31}k_{1y}, \quad (26)$$

where c_{11}, c_{22}, etc., are numerical coefficients to be determined. Experimental information allows us to make various choices for the values of these coefficients. In order to assign numerical values to all physical quantities involved in this problem, we have chosen some of them to be compatible with the observed wave-vector spectra,

$$c_{22}=-\tfrac{3}{2}, \quad c_{33}=-2, \quad c_{32}=-\tfrac{1}{2}, \quad (27)$$

and taking into account the matching condition, $\mathbf{k}_1+\mathbf{k}_2+\mathbf{k}_3=\mathbf{0}$, it is then possible to obtain the other coefficients as

$$c_{11}=\tfrac{7}{2}, \quad c_{31}=-\tfrac{1}{2}. \quad (28)$$

Plugging the information contained in Eqs. (27) and (28) into the relations (26), gives the following nondimensional values for the wave vectors:

$$k_{1x}=\tfrac{35}{2}, \quad k_{2x}=-\tfrac{15}{2}, \quad k_{3x}=-10, \quad (29)$$

$$k_{1y}=5, \quad k_{2y}=-\tfrac{5}{2}, \quad k_{3y}=-\tfrac{5}{2}. \quad (30)$$

As for the wave frequencies, we adopt a small frequency mismatch $\Delta\omega\ll\omega_2$ so as to keep the energy being interchanged among the coupled modes, and make the pump frequency ω_2 equal to the dominant poloidal frequency measured in the plasma edge fluctuations, viz. $\omega_{exp}=50$ kHz. In order to get nondimensional numbers we scale the frequencies by the ion-cyclotron frequency and obtain

$$\omega_1=\omega_2=\omega_3=1.31\times10^{-3}. \quad (31)$$

These frequencies enter the drift-wave dispersion relation (3), for $i=1,2,3$, as

$$\omega_i=\omega_{k_i}=-\frac{\mathcal{N}}{1+k_i^2}(\mathbf{k}_i\times\hat{\mathbf{z}})\cdot\hat{\mathbf{n}}, \quad (32)$$

where $\hat{\mathbf{n}}$ is a unit vector in the ∇n direction and (as previously noted) $\mathcal{N}=0.17$ is the quantity estimated in Eq. (25), after dividing by the Larmor radius ρ_s so as to yield a nondimensional number.

Because we are dealing with a $z=$constant plane, a plane perpendicular to the tokamak toroidal magnetic field, the gradient is $\nabla=\hat{\mathbf{x}}\partial/\partial x+\hat{\mathbf{y}}\partial/\partial y$ and

$$(\mathbf{k}_i\times\hat{\mathbf{z}})\cdot\nabla\ln\left(\frac{n_0}{\omega_{ci}}\right)\sim(\mathbf{k}_i\times\hat{\mathbf{z}})\cdot(\hat{\mathbf{x}}+\hat{\mathbf{y}})\mathcal{N},$$

and thus the dispersion relation simplifies to

$$\omega_i=\frac{(k_{iy}-k_{ix})}{1+k_i^2}\mathcal{N}. \quad (33)$$

Using the above, we can evaluate the coupling coefficient of Eq. (13) as

$$\Lambda_{2,3}^1 = \left(\frac{k_3^2 - k_2^2}{k_{1y} - k_{1x}}\right)(\mathbf{k}_2 \times \mathbf{k}_3) \cdot \hat{\mathbf{z}}$$

$$= \frac{\omega_1}{2\mathcal{N}} \frac{(k_{3x}^2 + k_{3y}^2 - k_{2x}^2 - k_{2y}^2)(k_{2x}k_{3y} - k_{3x}k_{2y})}{k_{1y} - k_{1x}}$$

$$= 32.8\omega_1. \tag{34}$$

With the frequencies given by (31), the numerical value for this coupling coefficient is seen to be $\Lambda_{2,3}^1 = 0.04$. Similarly, we obtain the other coupling coefficients of Eqs. (14) and (15),

$$\Lambda_{3,1}^2 = -421.8\omega_1 = -0.5, \quad \Lambda_{1,2}^3 = 335.9\omega_1 = 0.4. \tag{35}$$

Our estimation of the growth coefficients γ_i is based on the plasma turbulence levels in the tokamak edge region. We suppose that the pump mode (ϕ_2) induces the process of energy redistribution among the daughter modes ϕ_1 and ϕ_3. It would be unreasonable to have all three modes with positive growth rates, since this would lead to a nonphysical unbounded energy growth. Hence we suppose that the pump mode has a positive growth coefficient, whereas the daughter modes have negative growth rates. The numerical values have been adjusted to get wave-mode amplitudes in the range observed in experiments of plasma edge fluctuations, namely, -50 V – $+50$ V range for the floating potential measured with the electrostatic probe,[21] such that $\gamma_1 = \gamma_3 < 0$ and $\gamma_2 = 0.01$. We take γ_1 as the control parameter for the numerical simulations of Sec. V.

V. NUMERICAL RESULTS

Now we turn to the numerical evaluation of Eqs. (9)–(11) with the nondimensional parameter values introduced in Sec. IV: $\omega_1 = \omega_2 = \omega_3 = 0.001\,31$, $\gamma_1 = \gamma_3$, $\gamma_2 = 0.01$, $\Lambda_{2,3}^1 = 0.04$, $\Lambda_{3,1}^2 = -0.5$, and $\Lambda_{1,2}^3 = 0.4$. The wave modes $\phi_i(t)$ are complex numbers; hence, the phase space of this model has six dimensions. Because the growth and damping rates are included, there are no conserved quantities that can be used to reduce the effective number of degrees of freedom, and we expect very complex behavior to be observed in the numerical simulations. Also, phase-space volumes shrink with time with a constant rate given by $2(\gamma_1 - \gamma_2 - \gamma_3) < 0$. For all of our calculations we use the following six initial conditions for the real and imaginary parts of the modes:

$$\text{Re }\phi_1(0) = \text{Re }\phi_2(0) = \text{Re }\phi_3(0) = 0.1, \tag{36}$$

$$\text{Im }\phi_1(0) = \text{Im }\phi_1(0) = \text{Im }\phi_1(0) = 0.0. \tag{37}$$

The model equations (9)–(11) are integrated using a 12th-order Adams method from the LSODA (Livermore Solver for Ordinary Differential Equations) package.[26] We have observed both periodic and chaotic dynamics for the system trajectories, typical examples being shown in Fig. 1. A typical periodic trajectory is depicted in Fig. 1(a), where the dashed line indicates the pump wave amplitude $|\phi_2(t)|$ and the thin and thick full lines indicate the daughter wave amplitudes $|\phi_1(t)|$ and $|\phi_3(t)|$, respectively.

The pump wave, having a positive growth rate, initially increases exponentially at a rate consistent with the linear part of Eq. (9), because the other modes have amplitudes too small for the nonlinear term to play a significant role in the dynamics. However, as the other mode amplitudes increase, this linear growth is limited by the quadratic terms in Eq. (9), and the pump wave decays in an abrupt way imparting its energy to the daughter waves, which rapidly increase their amplitudes in spike-like events. Because the decay rates are different for each daughter, their maximum amplitudes turn out to be likewise different. On the other hand, since the time evolution of the daughter waves follow similar equations, their growth is also saturated by the nonlinear terms, and they also decay very fast, while the pump rises again completing the cycle.

The periodic behavior displayed in Fig. 1(a) can be conveniently viewed in a two-dimensional projection $[|\phi_1(t)|$ versus $|\phi_2(t)|]$ of the six-dimensional phase space [Fig. 1(b)], where the dynamics reveals a smooth limit cycle, with a period given by the time between two maxima of the pump amplitude, for example.

The existence of a well-defined period between events may not hold for other cases, however, as illustrated in Fig. 1(c), where the control parameter γ_1 has been changed from -0.100 to -0.211. In this case, the evolution of the three waves, although retaining the essential mechanism of linear growth saturated by nonlinear fast decay, seems to show no periodicity, since the time between consecutive maxima differs from event to event. The nature of the dynamics, again, can be inferred from the phase-space projection [Fig. 1(d)], which apparently shows a chaotic attractor. The existence of chaotic attractors in three-wave systems with quadratic nonlinearities has been long recognized as a typical feature.[10,11]

Because we are chiefly interested in the time evolution of the system, let us fix the spatial position by taking the arbitrary point $x = y = 0$ and consider the time series of the predicted electrostatic signal given by the sum of the three waves as in Eq. (16),

$$\phi(0,t) = \tfrac{1}{2}[\phi_1(t) + \phi_2(t) + \phi_3(t) + \text{c.c.}], \tag{38}$$

which can be dimensionalized, whenever necessary, by multiplying by the factor T_e/e [see Eq. (1)].

Figure 2(a) shows the time evolution of $\phi(0,t)$, which is the closest we can get, in the present model, to an experimental time series for the floating electrostatic potential, as measured by a probe. The parameters here are the same as in Fig. 1(d), so that it resembles a chaotic time series with floating potential in the range from -50 V to $+50$ V, with a histogram displaying a peaked distribution around zero [Fig. 2(b)]. To reinforce this conclusion, in Fig. 2(c) we plot the power spectral density of the signal shown in Fig. 2(a), which exhibits the broadband nature common to chaotic (and generally to random) systems. The spectrum clearly shows two time scales: a low frequency $f_2 \approx 30$ kHz, which is a result of our three-mode truncation model, and a main frequency peak $f_1 \approx 120$ kHz, which reflects the rate of energy interchange among the modes described by the model. The sideband peak to the left of the main peak f_1 comes from the linear combination $f_1 - f_2$ and is not directly related to the real dynamics.
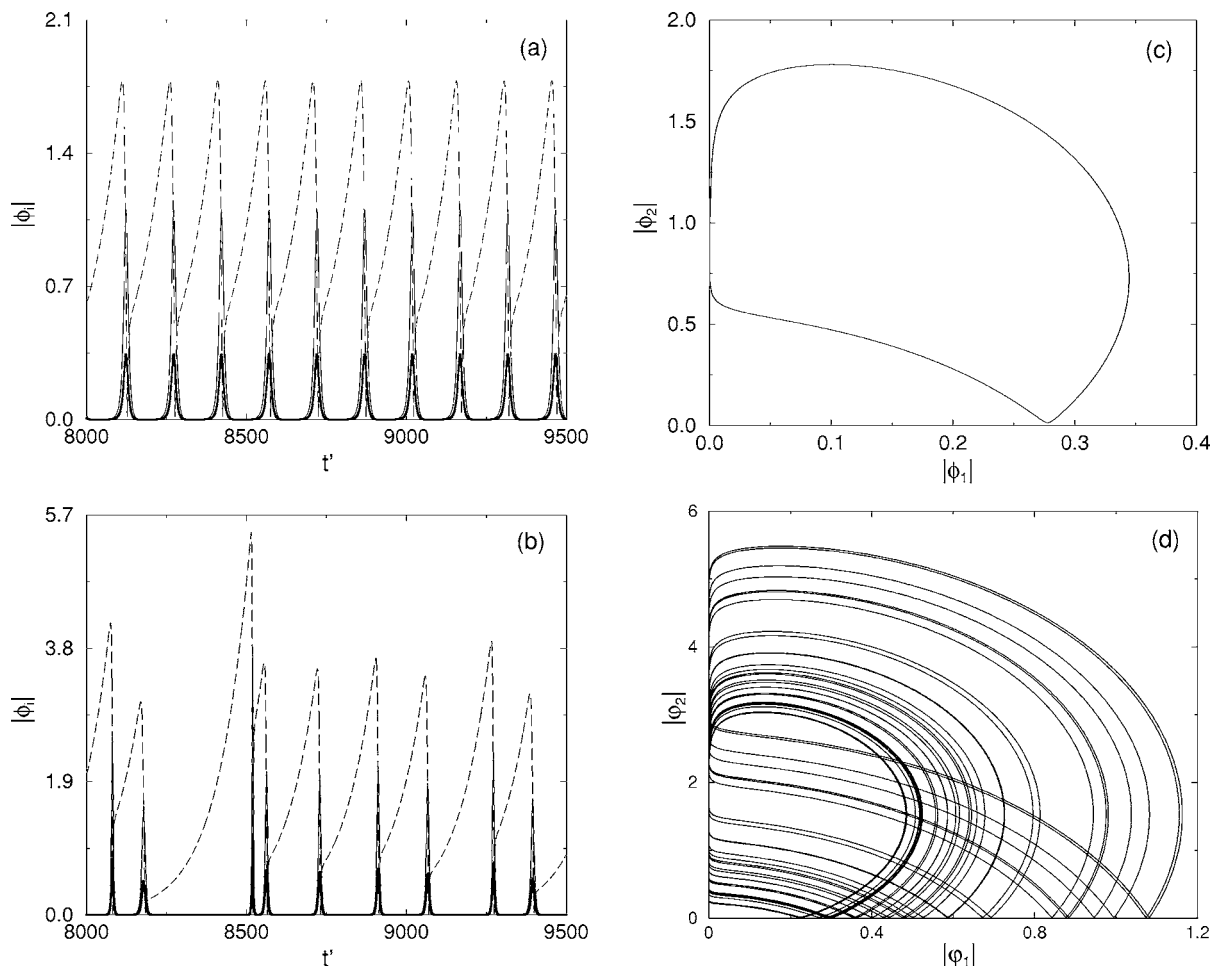
FIG. 1. (a) Time series of the wave amplitudes $|\phi_i|$ [$i=1$ (solid thin line), $i=2$ (dashed line), and $i=3$ (solid thick line)] for $\gamma_2=0.01$, $\omega_1=\omega_2=\omega_3$ $=0.001\,31$, and $\gamma_1=\gamma_3=-0.1$. (b) Same as (a) for $\gamma_1=\gamma_3=-0.211$. (c) The phase-space projection $|\phi_2|$ vs $|\phi_1|$ for the same γ's as in (a). (d) Same as (c) for $\gamma_1=\gamma_3=-0.211$.

The dependence of the dynamics on the control parameter γ_1 is illustrated by the bifurcation diagram shown in Fig. 3. This figure depicts the asymptotic values of the discrete variable $z_n:=\max|\phi_2|$, which is a stroboscopic map made from the time series of $\phi_2(t)$. Instead of sampling $\phi_2(t)$ at regular time intervals, we plot the values of $|\phi_2|$ at their local maxima. Qualitatively speaking, the stroboscopic plots are similar for both time periodic and local maxima sampling. Similar bifurcation diagrams could be obtained by considering the other wave amplitudes.

For values of γ_1 near -0.1, there is a fixed-point attractor in the stroboscopic plot, corresponding to a limit-cycle attractor such as that depicted in Fig. 1(a). As γ_1 becomes more negative, this attractor undergoes a period-doubling cascade that accumulates at $\gamma_1 \approx -0.19$, in a three-band chaotic attractor. These bands merge together into two larger bands possessing a period 6, which begins at $\gamma_c=-0.192\,669\,7$. Although barely visible in Fig. 3 due to insufficient graphical resolution, this periodic orbit evolves through an inverse period-doubling cascade as γ_1 increases in absolute value, eventually leading again to a two-band chaotic attractor which finally merges into a single-band attractor, such as that shown in Fig. 1(c).

We find that chaotic dynamics is typical as the absolute

value of γ_1 increases, as indicated by the wide chaotic band that extends to the leftmost part of the diagram, which is interspersed with periodic windows, with the most preeminent one being the period-3 window that starts at $\gamma_1 \approx -0.22$. The dynamics near these periodic windows has many features in common with an intermittent switching between laminar regions of periodic motion and chaotic bursts. Figure 4 illustrates such a situation for $\gamma_1=-0.192\,665$, a value slightly greater than γ_c.

The mechanism leading to this intermittency is a saddle-node bifurcation that occurs at $\gamma_1=\gamma_c$, which generates a pair of period-6 orbits with one stable and the other unstable. Taking into account the orbit period, we show in Fig. 5 a return plot of z_{n+6} versus z_n for the same value of γ_1 used in Fig. 4, i.e., for γ_1 slightly above the bifurcation point (the bifurcation occurs whenever the return plot crosses the diagonal). The sixth iterate map $z_{n+6}=f(z_n)$ presents a narrow channel with respect to the 45° line $z_{n+6}=z_n$, through which pass the trajectories comprising the periodic (laminar) intervals, after which the trajectory is randomly reinjected from the right to the left of the channel, forming the chaotic bursts observed in Fig. 4.

This bursting scenario is typical of the Pomeau-Manneville type-I intermittency, which occurs for one-
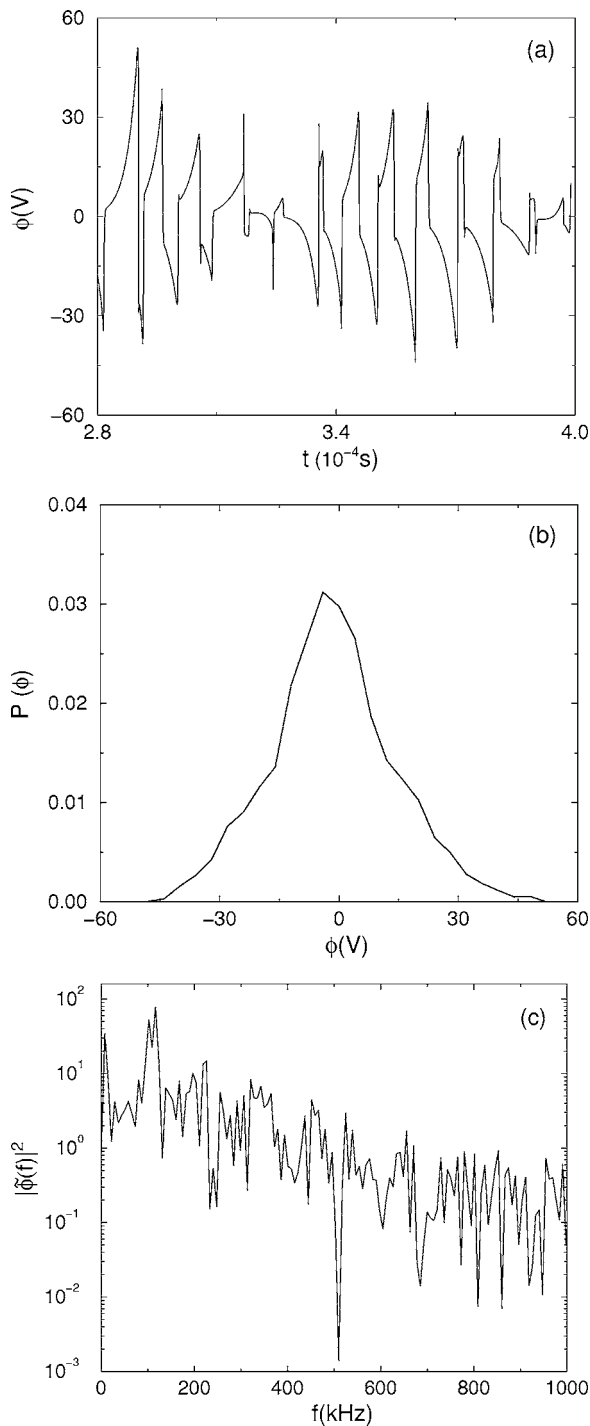
FIG. 2. (a) Time series of the potential in the real domain, $\phi(0,t)$, for the same parameters as those of Fig. 1(d). (b) Distribution of the corresponding values. (c) power spectrum of (a).
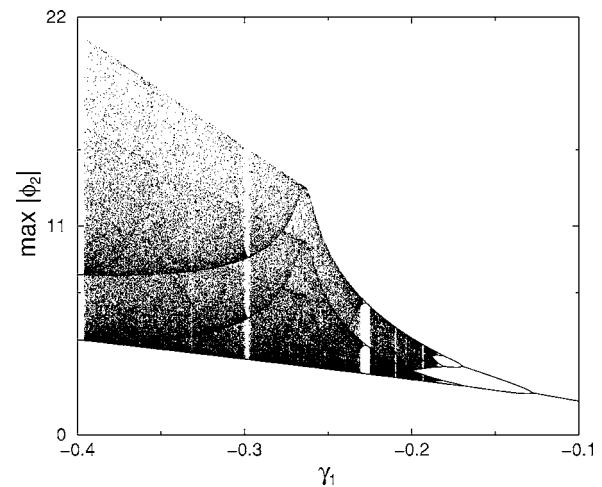

FIG. 3. Bifurcation diagram for the discrete variable $z_n := \max|\phi_2(t)|$ for varying $\gamma_1 = \gamma_3$. The remaining parameters are the same as in Fig. 1.

dimensional quadratic maps.[27] In fact, the existence of intermittent transitions to chaos has been long recognized as a typical feature of three-wave systems.[28] This shows that, at least in this case, the essential dynamics is one dimensional, in spite of its occurrence in the six-dimensional phase space.

VI. STATISTICS OF SPIKING EVENTS

Now we focus on the chaotic dynamics of z_n, for it displays a remarkable regularity in the statistical properties of the spiking events, which are related to the interchange of energy between modes. Figure 7 shows a magnification of a narrow time interval taken from the time series of the three waves, using the parameters of the chaotic attractor shown in Fig. 1(c). The dashed line represents the pump wave amplitude ϕ_2, which grows linearly until it reaches a threshold due to the quadratic nonlinearities, and then decays very fast. We have seen in the bifurcation diagram (Fig. 3) and in the ensuing figures that the local maxima $z_n = \max|\phi_2|$ coincide with the threshold points for sudden decay.
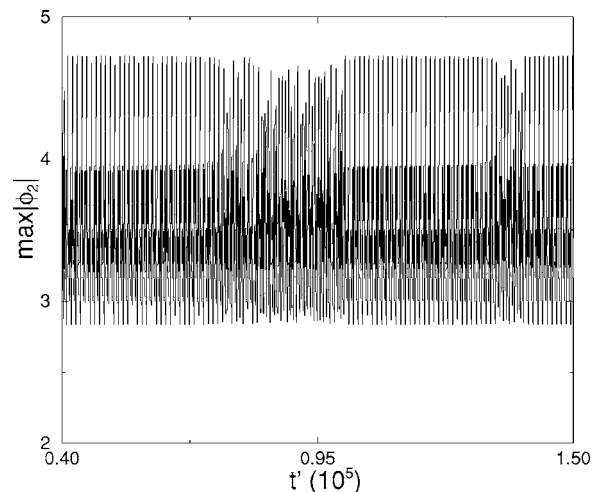

FIG. 4. Time series of the variable $z_n := \max|\phi_2(t)|$ for $\gamma_1 = -0.192\,665 \gtrsim \gamma_c$, illustrating an intermittent alternation between laminar periodic oscillations and chaotic bursts.

dimensional maps with quadratic extrema.[27] This can be also appreciated by computing the average duration of the laminar intervals, $\langle\sigma\rangle$, i.e., the average time between consecutive bursts. This calculation shows (see Fig. 6) that the average burst time scales as a power law according to

$$\langle\sigma\rangle \sim |\gamma_1 - \gamma_c|^{-\varpi}, \qquad (39)$$

where $\varpi = -0.511$. This value of ϖ is within numerical accuracy of the theoretically predicted value of $-1/2$ for one-
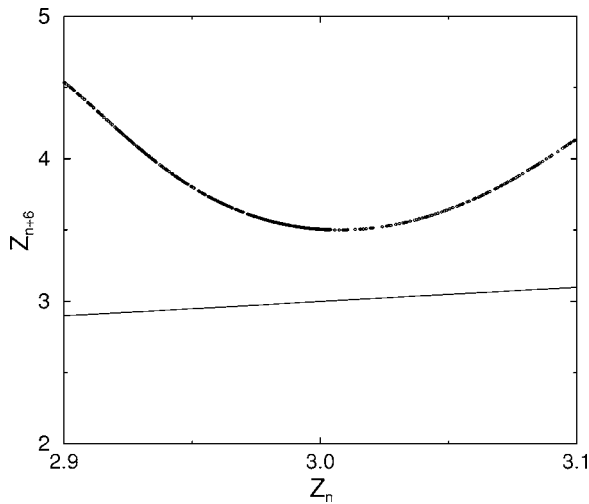
FIG. 5. Return plot for the sixth iterate map $z_{n+6}=f(z_n)$, for $\gamma_1=-0.192\,665 \gtrsim \gamma_c$, obtained from the time series of the variable $z_n := \max|\phi_2(t)|$ shown in Fig. 3. The straight reference line corresponds to the 45° line: $z_{n+6}=z_n$.

FIG. 7. Magnification of a narrow time interval of Fig. 1(b), illustrating the anatomy of a spiking event.

In the periodic (chaotic) regions of the bifurcation diagram the values of these thresholds vary in a regular (irregular) fashion with time. On the other hand, as the growth of the pump wave begins to saturate, there is a redistribution of energy to the daughter modes, depicted as the thick and thin solid lines in Fig. 7. Both modes grow fast with the decay of the pump mode and reach different maxima as the latter vanishes. As the process resumes, the daughter modes decay as the pump wave grows first with a fast nonlinear rate and then with a slower linear rate. During this second growth phase there is no interchange of energy between modes.

The spiking events, namely those occurring as the daughter modes ϕ_1 and ϕ_3 have nonvanishing amplitudes, are separated by different time intervals. Both daughter waves, while having different maxima, seem to be born and die at the same instants. We denote by τ the time interval that has elapsed between two spiking events. Numerically we treat wave amplitudes below a tolerance of $\approx 10^{-16}$ as van-
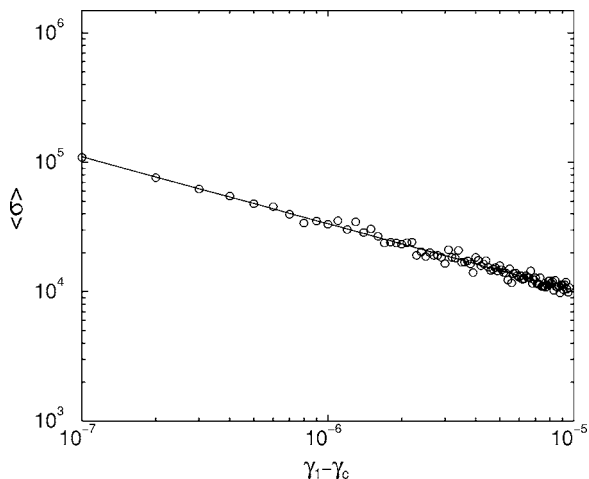
ishing. We have computed numerical approximations to the elapsed interval probability distribution $P(\tau)$, and our results are shown in Fig. 8 (in logarithmic scale) for different values of the control parameter γ_1. When the dynamics of z_n is chaotic [Fig. 8(a)] most of the interspike intervals are short and broadly distributed over a limited time range. In particular, it turns out that the largest interspike interval is around 300, with a roughly uniform distribution with peaks at the middle and ends of this interval.

As the parameter γ_1 increases in absolute value, the distribution remains broadband with an increase of both the maximum time interval and its average [Figs. 8(b) and 8(c)]. These facts can be qualitatively explained by considering that what ultimately determines the occurrence of a spike is the pump mode amplitude $|\phi_2|$ having reached the vicinity of a given threshold z_n, which depends on the nonlinearities present in the coupling between modes. For simplicity we assume that between spikes the pump mode growth is determined solely by its linear rate γ_2. Supposing that the linear growth begins at a certain value z^*, it follows that

FIG. 6. Average duration of laminar periodic oscillations for z_n and γ_1 in the immediate of vicinity a saddle-node bifurcation. The solid line is a least-squares fit with slope −0.5.
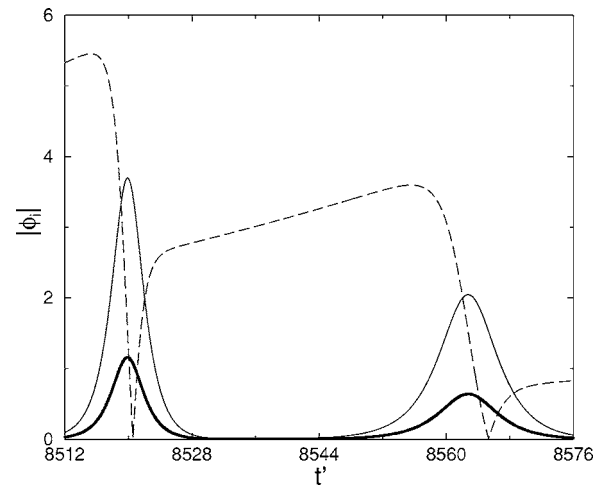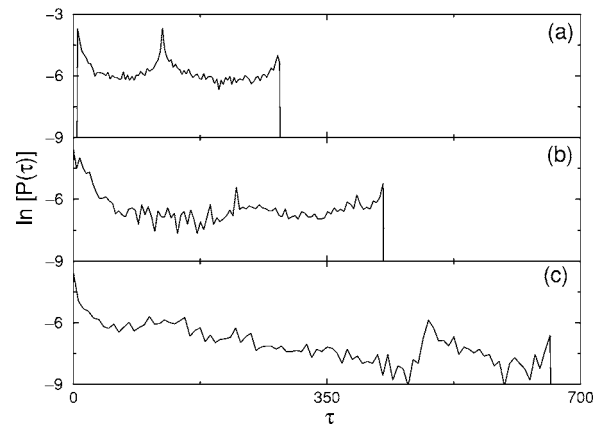

FIG. 8. Statistical distribution of the time interval between spiking events for γ_1 equal to: (a) −0.20; (b) −0.24; and (c) −0.26.
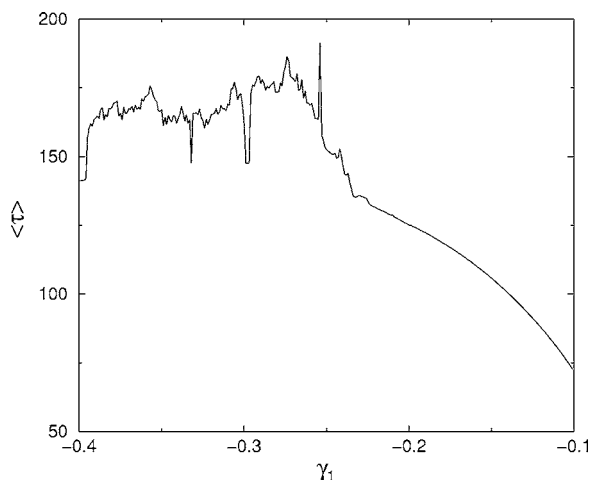
FIG. 9. Average interspike time interval as a function of γ_1.

$$z_n \sim z^* \exp(\gamma_2 \tau), \tag{40}$$

which indicates that a chaotic distribution of z_n will produce a likewise irregular distribution of τ.

The value of z^*, at which the linear growth of ϕ_2 begins, is of the same order of magnitude as the maxima of the daughter modes $\phi_{1,3}$, whose evolution is also influenced by the linear decay rates $\gamma_{1,3}$. If the daughter modes decay more rapidly, which occurs for lower values of γ_1, for example, it results in a lower value for z^* after which the inductor wave begins to grow. Lower values of z^* require higher interspike times τ for reaching similar thresholds z_n, so we expect the interspike intervals to grow with decreasing γ_1. In fact, if we plot the average interspike interval $\langle \tau \rangle$ as a function of γ_1, we observe that the average time grows monotonically with $-\gamma_1$ for values yielding periodic dynamics (Fig. 9).

On the other hand, the variation of $\langle \tau \rangle$ ceases to be smooth and becomes very peaked after the disappearance of the period-3 window at ≈ -0.22. The latter event is caused by a crisis, or the collision between the unstable period-3 orbit created at the beginning of the window, and the multiband chaotic attractor resulting from the small period-doubling cascade originating at the stable period-3 orbit. We currently have no explanation for this effect. Nevertheless, the average time seems to saturate for lower γ_1, in spite of this variation being smooth or peaked.

VII. CONCLUSIONS

Drift-wave turbulence is the major source of the irregular fluctuations observed in measurements of the floating potential at the tokamak plasma edge. A direct approach to drift-wave turbulence, to the extent it can be described by the Hasegawa-Mima equation, would be to consider a very large number of interacting modes and perform extensive computer simulations. A drawback of this approach is that one is never completely sure if the number of modes is large enough to reproduce the experimentally observed fluctuation spectra.

This paper has taken a different path, in that it emphasizes the basic building block of the turbulent cascade: the three-mode interaction. We have introduced in the original model proposed by Horton and others growth/decay rates and investigated their role in the resulting dynamics. We found that the decay rates of the daughter waves can be adjusted so as to yield a wide variety of dynamical behavior, ranging from simple periodicity to chaos, with different transition scenarios.

We have emphasized the type-I intermittency road to chaos, which is observed for a narrow interval of the growth rate and which can be responsible for the transition to turbulence actually observed in experiments. We also have found that the interval between spiking events, for which the pump and daughter waves actually interchange energy, have a strong dependence on the dynamics of the modes themselves, and a qualitative explanation has been given for the numerical results, based on the linear behavior.

Further work remains to be done to evaluate how useful the three-mode model for the driven-damped drift-wave equation is in comparison to models of fully developed turbulence. Terry and Horton show similar behavior for their multimode model.[19] In finite geometry, where the wavenumber spectrum is discrete and one mode has a dominant growth rate, the three-wave model is thought to give a faithful picture of the nonlinear system. In systems with many competing modes the key interaction for drift waves still occurs through the vector triad of Eqs. (9) and (10), so the solutions may well "shadow" the solutions of models with many modes. The details will differ as the amplitudes of the individual modes are reduced appreciably in the limit of a large number of modes.

[1] R. D. Hazeltine and J. D. Meiss, *Plasma Confinement* (Addison-Wesley, Reading, MA, 1992).

[2] R. Balescu, *Transport Processes in Plasmas: Classical Transport Theory* (North-Holland, Amsterdam, 1988).

[3] S. J. Camargo, B. D. Scott, and D. Biskamp, Phys. Plasmas **3**, 3912 (1996); S. J. Camargo, M. K. Tippett, and I. L. Caldas, Phys. Plasmas **7**, 2849 (2000).

[4] A. J. Wootton, S. C. McCool, and S. Zheng, Fusion Technol. **19**, 973 (1991); F. Wagner and U. Stroh, Plasma Phys. Controlled Fusion **35**, 1321 (1993).

[5] C. W. Horton, Rev. Mod. Phys. **71**, 735 (1999).

[6] Ch. P. Ritz, E. J. Powers, T. L. Rhodes, R. D. Bengtson, K. W. Gentle, H. Lin, P. E. Phillips, A. J. Wootton, D. L. Brower, N. C. Luhman Jr., W. A. Peebles, P. M. Schoch, and K. L. Hickok, Rev. Sci. Instrum. **59**, 1739 (1988).

[7] J. S. Kim, R. J. Fouck, R. D. Durst, E. Fernandez, P. W. Terry, S. F. Paul, and M. C. Zarnstortt, Phys. Rev. Lett. **79**, 841 (1997).

[8] A. Hasegawa and K. Mima, Phys. Rev. Lett. **39**, 205 (1977); Phys. Fluids **21**, 81 (1978).

[9] W. Horton and A. Hasegawa, Chaos **4**, 227 (1994).

[10] J. M. Wersinger, J. M. Finn, and E. Ott, Phys. Rev. Lett. **44**, 453 (1980); Phys. Fluids **23**, 1142 (1980).

[11] A. C.-L. Chian, S. R. Lopes, and M. V. Alves, Astron. Astrophys. **290**, L13 (1994); A. C.-L. Chian and J. R. Abalde, *ibid.* **298**, L9 (1995); S. R. Lopes and A. C.-L. Chian, Phys. Rev. E **54**, 170 (1996).

[12] I. L. Caldas, R. L. Viana, A. Vannucci, E. C. da Silva, M. S. T. Araujo, K.

Ullmann, M. V. A. P. Heller, and M. Y. Kucinski, Braz. J. Phys. **32**, 980 (2002).

[13]U. Frisch, *Turbulence* (Cambridge University Press, Cambridge, England, 1995).

[14]E. Ott, *Chaos in Dynamical Systems* (Cambridge University Press, Cambridge, England, 1993).

[15]A. Hasegawa, T. Imamura, K. Mima, and T. J. Taniuti, J. Phys. Soc. Jpn. **45**, 1005 (1978).

[16]K. Katou, J. Phys. Soc. Jpn. **51**, 996 (1982).

[17]G. I. de Oliveira, F. B. Rizzato, and L. P. L. de Oliveira, Physica D **104**, 119 (1997); R. Erichsen, L. G. Brunnet, and F. B. Rizzato, Phys. Rev. E **60**, 6566 (1999).

[18]E. N. Lorenz, J. Atmos. Sci. **20**, 130 (1963).

[19]P. Terry and W. Horton, Phys. Fluids **26**, 106 (1983); **25**, 491 (1982).

[20]I. C. Nascimento, I. L. Caldas, and R. M. O. Galvão, J. Fusion Energy **12**, 529 (1993).

[21]M. V. A. P. Heller, R. M. Castro, I. L. Caldas, Z. A. Brasilio, R. P. Silva, and I. C. Nascimento, J. Phys. Soc. Jpn. **66**, 3453 (1997).

[22]M. V. A. P. Heller, Z. A. Brasilio, I. L. Caldas, J. Stöckel, and J. Petrzilka, Phys. Plasmas **6**, 846 (1999).

[23]E. Mazzucatto, Phys. Fluids **21**, 1062 (1978).

[24]D. L. Brower, W. A. Peebles, and N. C. Luhmann, Phys. Rev. Lett. **54**, 689 (1985).

[25]R. M. Castro, M. V. A. P. Heller, I. L. Caldas, R. P. da Silva, Z. A. Brasilio, and I. C. Nascimento, Phys. Plasmas **3**, 971 (1996).

[26]A. C. Hindmarch, in *Scientific Computing*, edited by R. S. Stepleman *et al.* (North-Holland, Amsterdam, 1983), p. 55; L. R. Petzold, SIAM (Soc. Ind. Appl. Math.) J. Sci. Stat. Comput. **4**, 136 (1983).

[27]Y. Pomeau and P. Manneville, Commun. Math. Phys. **74**, 189 (1980).

[28]C. Meunier, M. N. Bussac, and G. Laval, Physica D **4**, 236 (1982).